

Central Lancashire Online Knowledge (CLoK)

Title	Effect of inter-layer spin diffusion on skyrmion motion in magnetic multilayers
Type	Article
URL	https://clock.uclan.ac.uk/29204/
DOI	https://doi.org/10.1038/s41598-019-46091-1
Date	2019
Citation	Lepadatu, Serban (2019) Effect of inter-layer spin diffusion on skyrmion motion in magnetic multilayers. <i>Scientific Reports</i> , 9 (1).
Creators	Lepadatu, Serban

It is advisable to refer to the publisher's version if you intend to cite from the work.
<https://doi.org/10.1038/s41598-019-46091-1>

For information about Research at UCLan please go to <http://www.uclan.ac.uk/research/>

All outputs in CLoK are protected by Intellectual Property Rights law, including Copyright law. Copyright, IPR and Moral Rights for the works on this site are retained by the individual authors and/or other copyright owners. Terms and conditions for use of this material are defined in the <http://clock.uclan.ac.uk/policies/>

SCIENTIFIC REPORTS



OPEN

Effect of inter-layer spin diffusion on skyrmion motion in magnetic multilayers

Serban Lepadatu

It is well known that skyrmions can be driven using spin-orbit torques due to the spin-Hall effect. Here we show an additional contribution in multilayered stacks arises from vertical spin currents due to inter-layer diffusion of a spin accumulation generated at a skyrmion. This additional interfacial spin torque is similar in form to the in-plane spin transfer torque, but is significantly enhanced in ultra-thin films and acts in the opposite direction to the electron flow. The combination of this diffusive spin torque and the spin-orbit torque results in skyrmion motion which helps to explain the observation of small skyrmion Hall angles even with moderate magnetisation damping values. Further, the effect of material imperfections on threshold currents and skyrmion Hall angle is also investigated. Topographical surface roughness, as small as a single monolayer variation, is shown to be an important contributing factor in ultra-thin films, resulting in good agreement with experimental observations.

Skyrmions are topologically protected particle-like magnetic textures¹, which are of great interest for potential technological applications. Skyrmions have been observed in materials with broken inversion symmetry and stabilised at room temperature through the Dzyaloshinskii-Moriya interaction (DMI)^{2–5}. As carriers of information it is important to effectively move, as well as detect, skyrmions using electrical signals and readout. To this end, recent experiments have revealed the fascinating physics behind the interaction of skyrmions with spin currents. Current-induced skyrmion movement was demonstrated at room temperature in a number of recent experiments on ultra-thin multilayered stacks^{6–12}, whilst electrical readout is made possible through the discrete Hall resistivity¹³. The principal source of spin currents in these devices is the spin-Hall effect (SHE), which converts a charge current flowing in the plane into transverse pure spin currents. The resultant spin-orbit torque (SOT) gives rise to skyrmion motion, with direction set by the charge current direction as well as skyrmion chirality¹⁴. The skyrmion Hall effect, whereby the direction of skyrmion movement deviates from that of the charge current direction due to the Magnus force, was also demonstrated^{8–10}. In some spintronics devices it is desirable to obtain zero skyrmion Hall angles, allowing for movement only along the current direction. Strategies to reduce the skyrmion Hall angle to zero have been proposed, using antiferromagnetically exchange-coupled bilayer systems¹⁵, antiferromagnetic skyrmions¹⁶, ferrimagnetic skyrmions^{11,17}, as well as using skyrmionium magnetic textures¹⁸.

Due to spin precession of spin-polarised electrons flowing through a magnetic texture, a spin accumulation is generated at magnetisation texture gradients resulting in adiabatic and non-adiabatic spin transfer torques (STT)^{19,20}. Furthermore spin diffusion was also shown to play a role, resulting in modified diffusive spin torques when considering two-dimensional magnetic textures²¹. On the other hand vertical spin currents have been shown to play a more important role in driving skyrmions in nanostructures²², whilst the importance of interfaces and interface-generated spin currents has also been recognised²³. Here we show, using micromagnetics modelling coupled with a self-consistent spin transport solver in multilayers, that the spin accumulation generated at the magnetisation gradients of a skyrmion results in additional vertical spin currents due to spin diffusion in adjacent non-magnetic layers. These diffusive spin currents result in additional interfacial spin torques which can be comparable to the SOT, significantly reducing the calculated skyrmion Hall angle even for small magnetisation damping values. In experiments it was found the skyrmion Hall angle strongly depends on the skyrmion velocity, evidencing the important role material imperfections play^{8–10}. Using the self-consistent spin transport solver we also study the effect of SOTs and inter-layer diffusion in the presence of magnetic defects, as well as topographical surface roughness. In particular surface roughness is shown to result in strong confining potentials, resulting in a dependence of the skyrmion Hall angle with driving current, as well as threshold current densities comparable

Jeremiah Horrocks Institute for Mathematics, Physics and Astronomy, University of Central Lancashire, Preston, PR1 2HE, UK. Correspondence and requests for materials should be addressed to S.L. (email: SLepadatu@uclan.ac.uk)

to those found in experiments. These results may indicate an alternative method of designing devices with zero skyrmion Hall angle, by purposely creating surface confining potentials.

Spin Transport Model

Spin torques included in the magnetisation dynamics equation can be computed self-consistently using a drift-diffusion model^{24,25}. Within this model the charge and spin current densities are given as:

$$\mathbf{J}_C = \sigma \mathbf{E} + \theta_{SHA} D_e \frac{e}{\mu_B} \nabla \times \mathbf{S} \quad (1)$$

$$\mathbf{J}_S = -\frac{\mu_B}{e} P \sigma \mathbf{E} \otimes \mathbf{m} - D_e \nabla \mathbf{S} + \theta_{SHA} \frac{\mu_B}{e} \epsilon \sigma \mathbf{E} \quad (2)$$

Here \mathbf{J}_S is a rank-2 tensor such that \mathbf{J}_{Sij} signifies the flow of the j component of spin polarisation in the direction i , \mathbf{J}_C is the charge current density, \mathbf{E} is the electric field, \mathbf{S} is the spin accumulation, and \mathbf{m} is the normalised magnetisation. Equation (2) contains contributions due to (i) drift included in ferromagnetic (F) layers, where P is the current spin-polarisation and σ the electrical conductivity, (ii) diffusion, where D_e is the electron diffusion constant, and (iii) spin-Hall effect, included in non-magnetic (N) layers, where θ_{SHA} is the spin-Hall angle and ϵ is the rank-3 unit antisymmetric tensor. The inverse spin-Hall effect is included for completeness as a contribution in Eq. (1). The spin accumulation satisfies the equation of motion:

$$\frac{\partial \mathbf{S}}{\partial t} = -\nabla \cdot \mathbf{J}_S - D_e \left(\frac{\mathbf{S}}{\lambda_{sf}^2} + \frac{\mathbf{S} \times \mathbf{m}}{\lambda_J^2} + \frac{\mathbf{m} \times (\mathbf{S} \times \mathbf{m})}{\lambda_\phi^2} \right) \quad (3)$$

Here λ_{sf} is the spin-flip length which governs the decay of spin accumulation. In F layers the decay of transverse components of \mathbf{S} are governed by the exchange rotation length λ_J , and the spin dephasing length λ_ϕ . Solving Eqs (1–3), we obtain a Poisson-type equation for the steady-state spin accumulation:

$$\nabla^2 \mathbf{S} = -\frac{P}{D_e} \frac{\mu_B}{e} (\mathbf{J}_C \cdot \nabla) \mathbf{m} + \frac{\theta_{SHA} \mu_B}{D_e e} \nabla \cdot (\epsilon \mathbf{J}_C) + \frac{\mathbf{S}}{\lambda_{sf}^2} + \frac{\mathbf{S} \times \mathbf{m}}{\lambda_J^2} + \frac{\mathbf{m} \times (\mathbf{S} \times \mathbf{m})}{\lambda_\phi^2} \quad (4)$$

Thus for each magnetisation configuration \mathbf{m} the resulting spin accumulation is obtained by solving Eq. (4). This is justified since \mathbf{m} and \mathbf{S} vary on very different timescales (ps vs fs respectively). In Equation (1) we have the usual relation $\mathbf{E} = -\nabla V$. For boundaries containing an electrode with a fixed potential, differential operators applied to V use a Dirichlet boundary condition. For other external boundaries we require both the charge and spin currents to be zero in the direction normal to the boundary²⁶, i.e. $\mathbf{J}_C \cdot \mathbf{n} = 0$ and $\mathbf{J}_S \cdot \mathbf{n} = 0$. This results in the following non-homogeneous Neumann boundary conditions:

$$\begin{aligned} \nabla V \cdot \mathbf{n} &= \theta_{SHA} \frac{D_e}{\sigma} \frac{e}{\mu_B} (\nabla \times \mathbf{S}) \cdot \mathbf{n} \\ (\nabla \mathbf{S}) \cdot \mathbf{n} &= \theta_{SHA} \frac{\sigma}{D_e} \frac{\mu_B}{e} (\epsilon \mathbf{E}) \cdot \mathbf{n} \end{aligned} \quad (5)$$

At the interface between two N layers we obtain composite media boundary conditions for V and \mathbf{S} by requiring both a potential and associated flux to be continuous in the direction normal to the interface, i.e. V and \mathbf{J}_C , and \mathbf{S} and \mathbf{J}_S respectively. At an N/F interface we do not assume such continuity, but instead model the absorption of transverse spin components using the spin-mixing conductance²⁷:

$$\begin{aligned} \mathbf{J}_C \cdot \mathbf{n}|_N &= \mathbf{J}_C \cdot \mathbf{n}|_F = -(G^\uparrow + G^\downarrow) \Delta V + (G^\uparrow - G^\downarrow) \Delta \mathbf{V}_S \cdot \mathbf{m} \\ \mathbf{J}_S \cdot \mathbf{n}|_N - \mathbf{J}_S \cdot \mathbf{n}|_F &= \frac{2\mu_B}{e} [\text{Re}\{G^{\uparrow\downarrow}\} \mathbf{m} \times (\mathbf{m} \times \Delta \mathbf{V}_S) + \text{Im}\{G^{\uparrow\downarrow}\} \mathbf{m} \times \Delta \mathbf{V}_S] \\ \mathbf{J}_S \cdot \mathbf{n}|_F &= \frac{\mu_B}{e} [-(G^\uparrow + G^\downarrow) (\Delta \mathbf{V}_S \cdot \mathbf{m}) \mathbf{m} + (G^\uparrow - G^\downarrow) \Delta V \mathbf{m}] \end{aligned} \quad (6)$$

Here ΔV is the potential drop across the N/F interface ($\Delta V = V_F - V_N$) and $\Delta \mathbf{V}_S$ is the spin chemical potential drop, where $\mathbf{V}_S = (D_e/\sigma)(e/\mu_B) \mathbf{S}$, and G^\uparrow, G^\downarrow are interface conductances for the majority and minority spin carriers respectively. The transverse spin current absorbed at the N/F interface results in a torque on the magnetisation as a consequence of conservation of total spin angular momentum. If the F layer has thickness d_F , this interfacial torque is obtained as:

$$\mathbf{T}_S = \frac{g\mu_B}{ed_F} [\text{Re}\{G^{\uparrow\downarrow}\} \mathbf{m} \times (\mathbf{m} \times \Delta \mathbf{V}_S) + \text{Im}\{G^{\uparrow\downarrow}\} \mathbf{m} \times \Delta \mathbf{V}_S] \quad (7)$$

In the equation of motion for \mathbf{m} , the interfacial torque is included as:

$$\frac{\partial \mathbf{m}}{\partial t} = -\gamma \mathbf{m} \times \mathbf{H}_{eff} + \alpha \mathbf{m} \times \frac{\partial \mathbf{m}}{\partial t} + \frac{1}{M_S} \mathbf{T}_S \quad (8)$$

Here $\gamma = \mu_0 g_{rel} |\gamma_e|$, where $\gamma_e = -g\mu_B/\hbar$ is the electron gyromagnetic ratio, g_{rel} is a relative g-factor, and M_s is the saturation magnetisation, such that $\mathbf{M} = \mathbf{m}M_s$ is the magnetisation vector. Using Eq. (6) we can also include spin pumping on the N side of the equation as²⁸:

$$\mathbf{J}_S^{pump} = \frac{\mu_B \hbar}{e^2} \left[\text{Re}\{G^{\uparrow\downarrow}\} \mathbf{m} \times \frac{\partial \mathbf{m}}{\partial t} + \text{Im}\{G^{\uparrow\downarrow}\} \frac{\partial \mathbf{m}}{\partial t} \right] \quad (9)$$

For an N/F interface with current in the plane, if diffusion effects are negligible, the drift-diffusion equations may be solved analytically to obtain the resulting interfacial spin torques due to SHE²⁵. These are given as a combination of damping-like and field-like spin-orbit torques as:

$$\mathbf{T}_{SOT} = \theta_{SHA, eff} \frac{\mu_B |J_c|}{e d_F} [\mathbf{m} \times (\mathbf{m} \times \mathbf{p}) + r_G \mathbf{m} \times \mathbf{p}] \quad (10)$$

Here $\mathbf{p} = \mathbf{z} \times \mathbf{e}_{jc}$, where \mathbf{e}_{jc} is the charge current direction. The quantity $\theta_{SHA, eff}$ is proportional to the real spin-Hall angle θ_{SHA} , scaled by transport and interface parameters, and is given by:

$$\theta_{SHA, eff} = \theta_{SHA} \left(1 - \frac{1}{\cosh(d_N/\lambda_{sf}^N)} \right) \frac{N_\lambda \text{Re}\{\tilde{G}\} + |\tilde{G}|^2}{(N_\lambda + \text{Re}\{\tilde{G}\})^2 + \text{Im}\{\tilde{G}\}^2}, \quad (11)$$

where $N_\lambda = \tanh(d_N/\lambda_{sf}^N)/\lambda_{sf}^N$, and $\tilde{G} = 2G^{\uparrow\downarrow}/\sigma_N$. The field-like torque coefficient is given by $r_G = N_\lambda \text{Im}\{\tilde{G}\}/(N_\lambda \text{Re}\{\tilde{G}\} + |\tilde{G}|^2)$. The self-consistent spin transport solver reproduces the SOT in Eq. (10), thus including both damping-like and field-like components. For simulations using the LLG equation complemented by the SOT in Eq. (10) directly, the calculated field-like and damping-like SOT coefficients must take into account the role of interface transparency²⁹ as given by the above equations.

With N/F multilayers another important source of vertical spin currents, resulting in an interfacial spin torque contribution, is due to N/F inter-layer diffusion of a spin accumulation generated in the F layer at spatial gradients in the magnetisation texture, e.g. a skyrmion. This is in some ways similar to the in-plane STT arising in the F layer alone^{19,20}, but in ultra-thin films the inter-layer diffusion results in much stronger spin torques partly due to the inverse dependence on d_F . It can be shown this additional interfacial spin torque is given by (see Supplementary Material for Derivation):

$$\mathbf{T}_{Diff.} = - \left[(\mathbf{u}_\perp \cdot \nabla) \mathbf{M} - \frac{\beta_\perp}{M_s} \mathbf{M} \times (\mathbf{u}_\perp \cdot \nabla) \mathbf{M} \right] \quad (12)$$

This interfacial spin torque has a very similar form to the well-known Zhang-Li STT, with the exception it acts in the opposite direction, i.e. results in motion along the current direction, and the spin-drift velocity and non-adiabaticity parameters are replaced by effective perpendicular spin-drift velocity and perpendicular non-adiabaticity parameters. In particular the perpendicular spin-drift velocity is given by:

$$\mathbf{u}_\perp = \mathbf{J}_c \frac{P_\perp g \mu_B}{2eM_s}, \quad (13)$$

where P_\perp is an effective perpendicular spin polarisation parameter. These parameters are not dependent on a single material alone, but are effective parameters for the entire multilayered stack.

Spin Torques in Multilayers

Current-induced Néel skyrmion movement has been observed in a number of ultra-thin multilayered stacks, including Ta/CoFeB/TaO_x^{6,9}, [Pt/Co/Ta]_x⁷, Ta/[Pt/Ir/Co]_x/Pt⁸, [Pt/CoFeB/MgO]_x^{7,10}, [Pt/GdFeCo/MgO]_x¹¹, and symmetric bilayer stacks¹². To study the effect of the spin torques described in the previous section on skyrmion motion, a multilayered disk geometry was chosen, with the structure [Pt (3 nm)\Co (1 nm)\Ta (4 nm)]_x, which has been well-characterised experimentally^{7,30-32}. The disk geometry was chosen so the influence of sample boundaries is the same irrespective of the skyrmion Hall angle. The studied geometry is shown in Fig. 1 for a repetition of 6 Pt/Co/Ta stacks ($x=6$). The bottom Pt layer was extended and a current applied to the structure through electrodes on its x-axis ends. This configuration ensures that, apart from the edges of the disks, the current density is approximately uniform (less than 2% variation in the region where skyrmion motion is simulated). A table with the full list of material parameters used is given in the Methods section.

First we investigate the effect of spin torques on a skyrmion in a single Pt/Co/Ta stack with fixed current density, for different chiralities and topological charges. Using a fixed out-of-plane field $|H_z| = 15$ kA/m the skyrmion diameter is fixed to 60 nm, similar to that observed experimentally⁷. The results are shown in Fig. 2. For the spin torque obtained with the self-consistent spin transport solver we see two distinct contributions. In addition to the spin torque due to SHE alone, namely SOT, an equally important contribution is obtained due to inter-layer spin diffusion. To demonstrate this, skyrmions have been driven with and without SHE contribution. Without SHE ($\theta_{SHA} = 0$ in both Pt and Ta) the only torque acting on the skyrmions is due to inter-layer spin diffusion, as seen from the good agreement between spin transport solver computations with $\theta_{SHA} = 0$, and simulations using the LLG equation complemented by the diffusive spin torque in Eq. (12). The vertical spin current due to diffusion is shown in the Pt layer in Fig. 1, as well as the resulting interfacial spin torque acting on the skyrmion. Note, in this

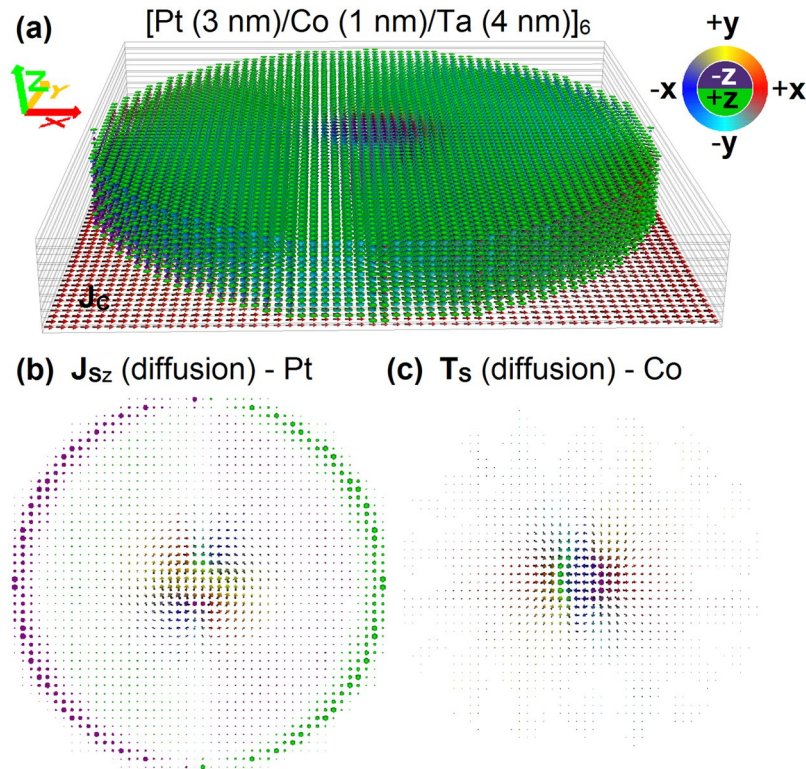


Figure 1. (a) Multilayered $[\text{Pt}/\text{Co}/\text{Ta}]_6$ 320 nm diameter disk with a Néel skyrmion, showing the charge current density injected through the bottom Pt layer. The direction of vector quantities, as represented by arrows, is also color encoded as shown by the color wheel. The images below show (b) the z-direction spin current density in a Pt layer, as generated due to inter-layer spin diffusion, as well as (c) the resulting spin torque on a Co layer.

work we didn't consider Zhang-Li in-plane STTs since their effect is much smaller in ultra-thin films compared to interfacial spin torques²².

For Equation (12) we find $P_{\perp} = 0.87$ and $\beta_{\perp} = -0.13$ for the interfacial spin torque. The large effective perpendicular spin polarisation and perpendicular non-adiabaticity parameters result in a total spin torque comparable to the SOT. In contrast to SOTs however, the direction of motion is opposite to the electron flow in all cases, for both $D < 0$ and $D > 0$, where D is the DMI exchange constant. Further, by subtracting results obtained using the spin transport solver for $\theta_{\text{SHA}} \neq 0$ and $\theta_{\text{SHA}} = 0$ we obtain a good agreement with simulations using the LLG equation complemented by the SOT in Eq. (10). As expected, with the SOT alone the direction of motion depends on the sign of the DMI. However, when inter-layer spin diffusion is taken into account, the overall effect is for skyrmion motion opposing the flow of electrons in all cases.

Experimental investigations of current-induced skyrmion movement have revealed skyrmion displacement in the direction opposing the flow of electrons^{6–12}, and these results have been analysed principally based on the SOT due to SHE. We show here however, inter-layer spin diffusion could also have a significant effect and should be considered when analysing skyrmion motion. The implications are both qualitative and quantitative. Since the skyrmion motion direction due to the diffusive spin torque is always in the direction opposing the flow of electrons, if inter-layer spin diffusion is significant, the exact topology of skyrmions cannot be determined purely based on observing their motion direction (with or against the electron flow). Quantitatively, whilst the skyrmion velocities are not greatly affected by inclusion of the diffusive spin torque, due to the nearly orthogonal skyrmion movement directions under these two torques respectively, the skyrmion Hall angle obtained varies markedly and could have significant implications in explaining experimental results. To experimentally verify the interfacial diffusive spin torque directly, material stacks having both low total SOT and high DMI could be used, whilst still preserving the lack of inversion symmetry required for stable skyrmions; moreover the metallic underlayers used should be good spin sinks (small spin diffusion length) in order to maximise the diffusive spin torque. This presents a materials engineering challenge since SHE and DMI strengths tend to be correlated. One suggested possibility is to use interface doping to change the efficiency of the SOT^{33,34}, and it is hoped the results shown here will stimulate further experimental work.

The Onsager reciprocal process to absorption of transverse spin currents is the generation of spin currents via dynamical magnetisation processes, known as spin pumping²⁸ – see Eq. (9). The effect of spin pumping on magnetisation precession is an increase in the effective magnetisation damping. As expected from the Thiele equation³⁵, larger damping values should result in reduced skyrmion velocities, thus it is interesting to observe its effect on skyrmion motion. First we keep the current density fixed, and later analyse the effect of varying the current density. With spin pumping enabled in the spin transport solver, a spin drag effect is observed, resulting

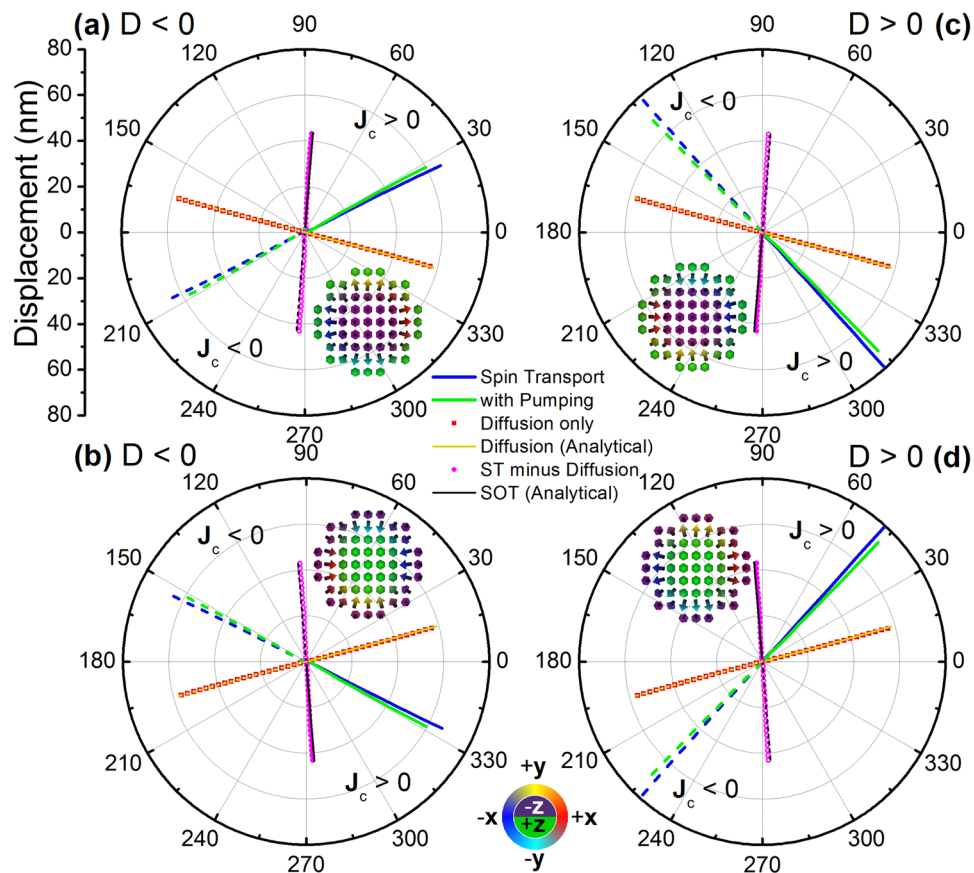


Figure 2. Néel skyrmion motion in a Pt/Co/Ta disk shown for $J_C = \pm 1.3 \times 10^{11}$ A/m², $D = \pm 1.5$ mJ/m² and different skyrmion core orientations: into the plane for (a,c) with applied field $H_z = 15$ kA/m, out of the plane for (b,d) with $H_z = -15$ kA/m. The insets represent the respective skyrmions with arrow directions indicated by the color wheel at the bottom. The skyrmion motion is shown for the self-consistent spin transport solver (blue lines), spin transport solver including spin pumping (green lines), spin transport solver but without SHE, thus with vertical spin currents due to inter-layer spin diffusion only (red squares). The latter is compared with simulations using the analytical form of the diffusive spin torque (yellow lines) – Eq. (12). The difference between spin transport solver results for cases with and without SHE is shown as magenta circles. This is compared with results using the analytical form of the SOT (black lines) – Eq. (10). Solid lines and symbols are for $J_C > 0$, whilst dashed lines and open symbols are for $J_C < 0$.

in a slight reduction in velocity as shown in Fig. 2, as well as a slight deviation of the skyrmion path. This effect is quite small however and could be ignored in simpler simulations using only the analytical form of the SOT and diffusive spin torque.

The results discussed thus far used an intrinsic damping value in Co of 0.03, as obtained using ferromagnetic resonance measurements in ultra-thin films³⁶. On the other hand, much higher damping values of up to 0.3 have been obtained in Pt/Co/Pt films from magnetic domain-wall motion experiments³⁷. Increasing damping results in a reduced skyrmion velocity as expected, however more significantly the direction of motion is strongly affected, resulting in a clockwise rotation of the skyrmion paths with increasing damping as seen in Fig. 3. This holds for both the SOT and diffusive spin torque, and again a good agreement is obtained between the spin transport solver results and simulations using the analytical forms of the SOT and diffusive spin torque. Small skyrmion Hall angles have been observed experimentally^{9,10}. Based on the SOT alone the skyrmion Hall angle is inversely dependent on the magnetisation damping³⁸, namely $\tan \theta_{skH} \propto 1/\alpha$, and as noted in ref.¹⁰ the experimentally observed skyrmion Hall angles are smaller than those obtained using micromagnetics modelling with the SOT alone, under realistic parameters. As shown in ref.⁹ disorder plays a very significant effect on the skyrmion Hall angle, particularly in explaining its dependence on the skyrmion velocity, and this aspect is also analysed in this work in the following section. The results in Fig. 3 show that inclusion of diffusive spin torque can result in small skyrmion Hall angles even at moderate magnetisation damping values. We propose here the diffusive spin torque may help to explain the experimentally observed small skyrmion Hall angles and it is hoped these results will encourage further work in this direction.

Increasing the number of stack repetitions results in modified demagnetising fields, and these are known to have an effect on skyrmion motion under a SOT^{22,39,40}. In particular multilayered stacks can accommodate hybrid skyrmion structures^{39,40} where the chirality changes with layer number. For the Pt/Co/Ta stacks studied here, with

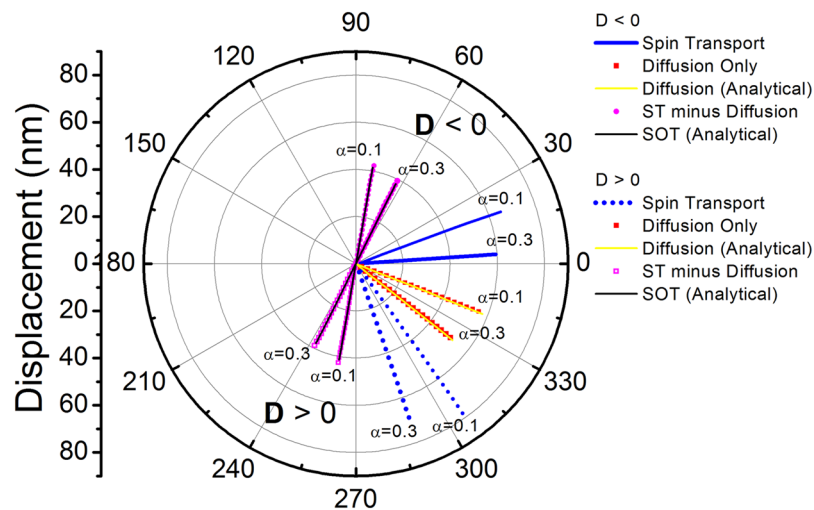


Figure 3. Effect of higher damping values on skyrmion motion under various spin torques for $J_C = 1.3 \times 10^{11} \text{ A/m}^2$, $H_z = 15 \text{ kA/m}$, and $D = \pm 1.5 \text{ mJ/m}^2$. Solid lines and symbols are for $D < 0$, whilst dashed lines and open symbols are for $D > 0$.

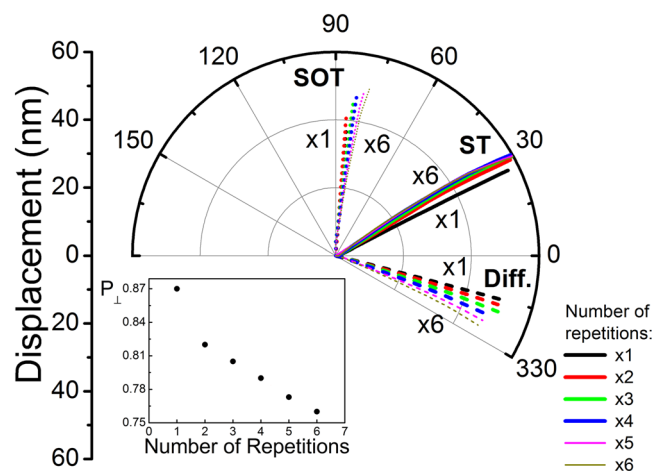


Figure 4. Néel skyrmion motion in $[\text{Pt}/\text{Co}/\text{Ta}]_x$ disks ($x = 1, \dots, 6$) shown for $J_C = 1.3 \times 10^{11} \text{ A/m}^2$, $D = -1.5 \text{ mJ/m}^2$ with $H_z = 15 \text{ kA/m}$. Results obtained using the self-consistent spin transport solver are shown with SHE (ST) and without SHE (Diff.). These results are contrasted with simulations using only the analytical form of the SOT. The effect of inter-layer spin diffusion on skyrmion motion is dependent on the number of Pt/Co/Ta repetitions, as is the SOT. The combined effect however saturates after 3 repetitions in this case (ST). The inset shows the calculated perpendicular effective spin polarisation parameter as a function of number of stack repetitions. The perpendicular effective non-adiabaticity parameter is not affected by the number of repetitions.

relatively large spacing between the Co layers, we have verified the chirality does not change along the thickness (see Supplementary Material for details). Additionally, the total effective diffusive spin torque is affected by the number of repetitions in the multilayered stack. The spin accumulation generated at a skyrmion diffuses across the Pt and Ta layers, with the transverse components of the spin current absorbed in neighbouring Co layers. Due to the symmetry of the structure, a decrease in the overall diffusive spin torque is expected, reflected in a decrease of the effective perpendicular spin polarisation parameter P_{\perp} . The results for stacks with up to 6 number of repetitions are shown in Fig. 4. With a single stack repetition the only contribution to the total effective diffusive spin torque is the main contribution due to diffusion from the Co layer into the adjacent Pt and Ta layers. From 2 stack repetitions up we have the additional contributions due to diffused spin currents between adjacent Co layers – with 2 stacks each Co layer has contributions due to the other Co layer only; with 3 stack repetitions up, the inner Co layers experience contributions from the 2 adjacent layers. The total effect is a decrease in the total effective diffusive spin torque as the number of layers is increased – this is reflected in the decrease of P_{\perp} as shown in the inset to Fig. 4. Further details are given in the Supplementary Material, where the current densities through the multilayered stack are also shown. It is interesting to note that as the number of repetitions is increased, the total spin torque, consisting of the combination of SOT and diffusive spin torque, results in the same skyrmion motion

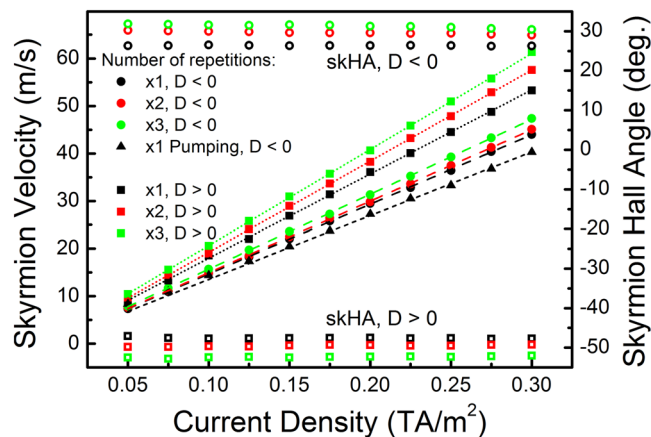


Figure 5. Single skyrmion velocities in $[\text{Pt}/\text{Co}/\text{Ta}]_x$ disks ($x = 1, 2, 3$) obtained as a function of current density for $D = \pm 1.5 \text{ m}^2/\text{m}^2$ with $H_z = 15 \text{ kA}/\text{m}$, are shown as solid symbols together with linear fits (left hand side scale). The skyrmion Hall angles (skHA) are shown as open symbols with color coding corresponding to the number of Pt/Co/Ta repetitions, both for $D < 0$ and $D > 0$ (right hand side scale). Velocities obtained with spin pumping enabled are shown as triangles.

above 3 repetitions – thus for $x = 4, 5, 6$ the skyrmion paths and velocities are nearly identical, as seen in Fig. 4. It must be stressed however this is not generally true since the skyrmion motion is a result of the interplay between the spin torques and demagnetising fields.

Finally, before analysing the effect of defects on skyrmion motion and threshold currents, the velocities are computed in perfect structures using the self-consistent spin transport solver. The results for up to 3 stack repetitions for both $D < 0$ and $D > 0$ are shown in Fig. 5. Due to the symmetry of the various spin torques (see Fig. 2) the velocities for $D > 0$ are greater than for $D < 0$, and moreover the motion in both cases opposes the drift direction of electrons. The skyrmion reaches its steady velocity almost instantaneously in these disk structures – any acceleration period is below the numerical error. The velocities obtained are very similar to those obtained in experiments on similar stack compositions with similar skyrmion diameters⁷. It must be stressed however that a precise comparison is difficult largely due to the unknown skyrmion Hall angle. Moreover the movement of skyrmions is also affected by the shape anisotropy of track structures, and disorder plays a very significant effect on the skyrmion movement path. Comparable skyrmion velocities have also been observed in other experimental studies^{10–12}, although the stack compositions are different. When spin pumping is also taken into account, a small decrease in velocity is observed in Fig. 5 which is proportional to the driving current. This is explained as an increased spin drag effect as the skyrmion velocity increases, resulting in larger pumped spin current in Eq. (9).

Threshold Currents

Experimental results on current-induced skyrmion motion show the existence of threshold currents required to initiate and sustain motion^{7–12}. Further, the skyrmion Hall angle has been found to vary with skyrmion velocity^{8–10}. These effects are difficult to explain using simulations with perfect structures and constant material parameters. Material imperfections seem to play a very significant role in explaining these experimental observations. Previous studies have shown how a threshold current arises due to confining pinning potentials^{41,42}, defect scattering^{43,44}, polycrystalline structures with crystallites of varying anisotropy axes orientation⁴⁵, disorder originating from M_S fluctuations using a granular structure⁴⁶, as well as disorder in the DMI^{7,8} and anisotropy constant^{7,11}. Imperfections have also been shown to result in a change of the skyrmion Hall angle with skyrmion velocity due to sliding motion along grain boundaries⁴⁵. Another mechanism which results in variation of the skyrmion Hall angle with velocity is due to the field-like SOT component in combination with breathing skyrmion modes^{47,48}, or deformations and internal mode excitations¹⁰. The field-like SOT in Eq. (10) has also been included in this work. Moreover Brownian motion of skyrmions due to thermal effects can result in distortions and diffusion of skyrmions^{49,50}.

Here we consider, in addition to variations of M_S and K_u parameters, also the effect of topographical surface roughness, included in simulations as a roughness field^{51,52}. Topographical surface roughness results in an effective uniaxial anisotropy when averaged over the entire sample, however locally the roughness field has strong variations, which can result in confining potentials due to local fluctuations of the total effective anisotropy. Since the Co layers are very thin, variations in thickness of even a single monolayer can result in strong confining potentials. In this work we consider the effect of surface roughness up to 2 \AA roughness per surface which is comparable to a single monolayer thickness variation. Roughness textures are generated as jagged granular profiles (see Methods section) with a 50 nm grain size, as shown in Fig. 6 for topographical surface roughness. It is known that threshold currents depend on the skyrmion diameter to grain size ratio, with the strongest pinning obtained when this ratio is close to unity⁸. Here we keep the grain size fixed in order to investigate threshold currents and variation of the skyrmion Hall angle. Further analysis using combinations of various sources of imperfections as well as grain size variation is outside the scope of the current work.

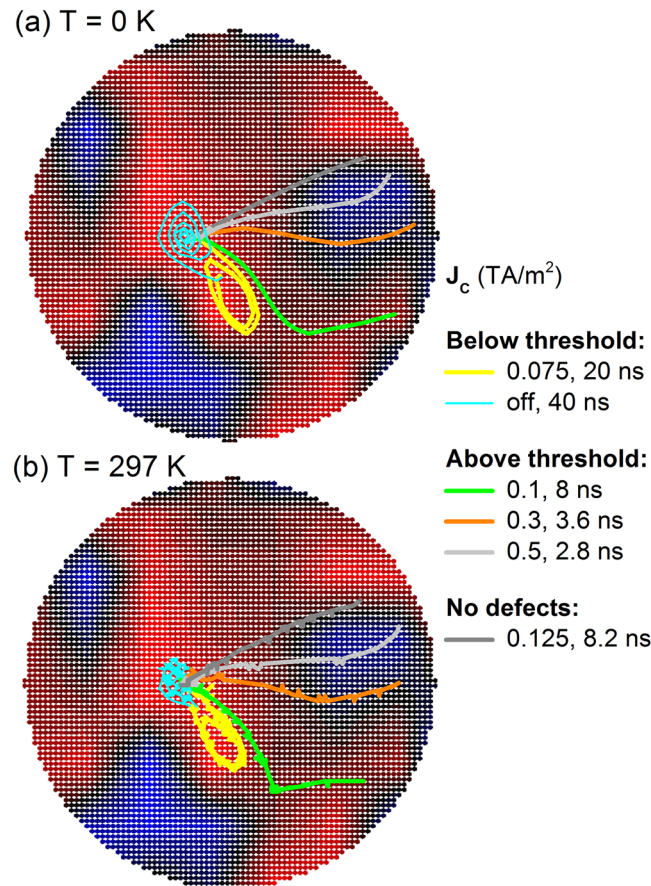


Figure 6. Effect of 2 Å surface roughness in a 320 nm diameter disk (plotted using color coding, ranging from blue at maximum depth of 2 Å to red), on skyrmion motion for various current densities, for both (a) 0 K, and (b) 297 K with thermal fluctuations. The skyrmion is initially at a confining site. Below the threshold current the skyrmion orbits within the confining site and is unable to escape. When the current is turned off the skyrmion returns to its initial position. Just above the threshold current the skyrmion escapes the confining site but its motion direction is strongly influenced by the local roughness profile, following a path with largest magnetic layer thickness. As the current density is increased the skyrmion path tends towards that obtained without surface roughness.

Results for skyrmion motion using surface roughness are shown in Fig. 6, both for zero temperature and room temperature. For the latter a thermal field was also introduced as outlined in the Methods section. For the simulations in this section the skyrmion was relaxed into a confining site, then current densities of various strengths were applied and the skyrmion motion was computed using the full spin transport solver. For small current densities the skyrmion tends to undergo an orbiting motion inside the confining potential, as shown in Fig. 6. As soon as the current is turned off, the skyrmion relaxes back to the initial position, representing the lowest energy configuration inside the two-dimensional confining potential. As the current is increased, eventually the skyrmion is able to escape. The calculated threshold current of 10^{11} A/m² for 2 Å surface roughness is very similar to that found in experiments⁷. The skyrmion motion is strongly influenced by the local roughness profile and can differ considerably from that obtained in perfect structures. With surface roughness the skyrmion tends to follow a path with greatest layer thickness, since this represents the lowest energy path. As the current density is increased the skyrmion path tends towards that obtained in perfect structures, as shown in Fig. 6. Whilst the movement direction is strongly affected by the local roughness profile, the average skyrmion velocity above the threshold current is similar to that obtained in perfect structures, as seen in Fig. 7(a), especially for the full spin transport solver results which include both the SOT and interfacial diffusive spin torque. The skyrmion velocity shown in Fig. 7(a) was also obtained separately using these two contributions; with the interfacial diffusive spin torque alone is close to the lowest energy path direction on average – compare the low current-density path in Fig. 6 with that obtained under the diffusive interfacial spin torque alone in Fig. 2(a). When a stochastic thermal field is introduced for room-temperature simulations the skyrmion paths are largely unaffected, showing only a small random variation around the path taken without a thermal field. The threshold current is also unaffected. This suggests the additional Brownian motion of skyrmions, including diameter variations due to thermally-excited breathing modes, is insufficient to overcome the pinning potentials in this case.

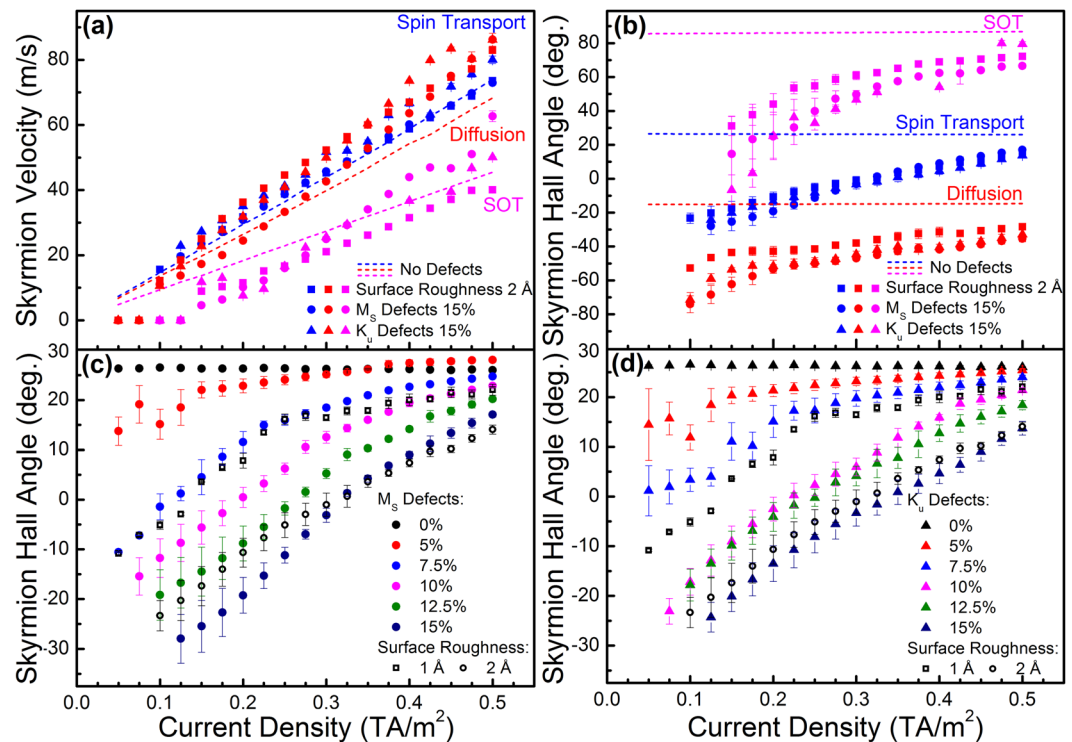


Figure 7. Skyrmion velocities and skyrmion Hall angles for various defect types, including M_S and K_u variations up to 15%, as well as surface roughness up to 2 Å per surface, showing (a) velocities as a function of current density, and (b) average skyrmion Hall angles as a function of current density, for spin transport solver results with SHE (Spin Transport) and without SHE (Diffusion), as well as simulations using only the analytical form of the SOT. Panels (c) and (d) show detailed average skyrmion Hall angle variation calculated using the full spin transport solver as a function of current density and defect strength.

We further study the effect of magnetic defects, in particular considering variation of M_S and K_u parameters by changing the variation amplitude from 5% up to 15%. The results are shown in Fig. 7. As expected, increasing the variation amplitude results in increasing threshold currents, with the largest threshold currents obtained for 15% variation as 1.25×10^{11} A/m², comparable to that obtained for 2 Å surface roughness. It is unclear if such a strong parameter variation amplitude is likely in good quality samples, however a single monolayer variation at surfaces is possible, particularly in multilayered stacks considering the size of typical samples used to study skyrmion motion. The average skyrmion Hall angle is plotted in Fig. 7(c,d) as a function of both current density and parameter variation amplitude. As the current density is increased the skyrmion Hall angle tends to that obtained in the ideal structure, levelling off as the current density is increased. This behaviour is also observed under the SOT and diffusive interfacial spin torque separately as shown in Fig. 7(b). Such a strong influence of the skyrmion velocity on its motion direction has also been observed in experimental studies^{8–10}. Moreover, imaging of multiple skyrmions movement has shown simultaneously both negative and positive skyrmion Hall angles within the same driving current pulse⁸. The results in Fig. 7 show how the sign of the skyrmion Hall angle can change depending on the level of disorder, as well as the driving current density, highlighting the effect local disorder can have on skyrmion movement.

Here we showed that in addition to magnetic defects, topographical surface roughness also plays a very important part. The results on surface roughness show it may be possible to design devices with skyrmion motion only along the current direction, by purposely enlarging the thickness of the structure in the center. This creates a strong confining potential in the center, whilst avoiding the sample boundaries, without significantly affecting the skyrmion speed. It is hoped these results will further stimulate experimental work in this direction.

Conclusions

In conclusion, we have studied single skyrmion motion in ultra-thin multilayered Pt/Co/Ta disks by means of micromagnetics simulations coupled with a self-consistent spin transport solver. Vertical spin currents can drive skyrmions very efficiently in such structures. One source of vertical spin currents is the SHE, resulting in SOTs acting on the Co layers. Another source of vertical spin currents was shown here, resulting from inter-layer diffusion of a spin accumulation generated at a skyrmion. This diffusive spin torque was shown to act in the direction of electrical current irrespective of the skyrmion chirality or topological charge, and in ultra-thin films can be comparable to the SOT. The combination of SOT and diffusive spin torque was found to result in small skyrmion Hall angles even for small magnetisation damping values. Further, the effect of magnetic defects and topographical surface roughness on the skyrmion Hall angle and threshold current was studied. In particular topographical

Parameter	Value	References
$ D $ (Co)	1.5 mJ/m ²	7
M_S (Co)	600 kA/m	7
A (Co)	10 pJ/m	7
K_u (Co)	380 kJ/m ³	7
α (Co)	0.03 up to 0.3	resp ^{36,37} .
g_{rel} (Co)	1.3	36
σ (Co)	5 MS/m	56
σ (Pt)	7 MS/m	29
σ (Ta)	500 kS/m	57
P (Co)	0.4	58,59
De (Co, Pt, Ta)	0.01 m ² /s	56
λ_{sf} (Co)	38 nm	56,60
λ_{sf} (Pt)	1.4 nm	29
λ_{sf} (Ta)	1.9 nm	57
λ_J (Co)	2 nm	20
λ_φ (Co)	4 nm	54,55
G^{\perp} (Pt/Co)	1.5 PS/m ²	29
G^{\perp} (Co/Ta)	1 PS/m ²	57
θ_{SHA} (Pt)	0.19	29,30
θ_{SHA} (Ta)	-0.15	30,61

Table 1. Material parameters used to model the Pt/Co/Ta stacks.

surface roughness, as small as a single monolayer variation, was shown to have a marked effect, resulting in a dependence of the skyrmion Hall angle on the skyrmion velocity, with threshold currents comparable to those found in experiments.

Methods

All simulations were done using Boris Computational Spintronics software⁵³, version 2.2. Material parameters used in the simulations are summarised in Table 1.

In Table 1 the spin dephasing length is given is given by $\lambda_\phi = \lambda_J \sqrt{l_\perp / l_L}$, where l_\perp and l_L are the transverse spin coherence and spin precession lengths respectively^{54,55}, estimated as 4 nm for Co.

Computations were done using cell-centered finite difference discretisation. Differential operators are evaluated to second order accuracy in space, for both magnetisation and spin transport calculations. For magnetisation dynamics the computational cellsize used was (4 nm, 4 nm, 1 nm). For spin transport calculations the computational cellsize used was (4 nm, 4 nm, 0.5 nm) for the Pt and Ta layers, and (4 nm, 4 nm, 0.25 nm) for the Co layers. The LLG equation was evaluated using the RK4 evaluation with a 0.5 ps fixed time step. The Poisson equations for spin and charge transport, e.g. Eq. (4) for S , were evaluated using the successive over-relaxation algorithm. All computations were done on the GPU using the CUDA C framework.

In the LLG equation the contributing interactions are the demagnetising field, direct exchange interaction, the interfacial Dzyaloshinskii-Moriya exchange interaction, uniaxial magneto-crystalline anisotropy and applied field. The roughness field resulting from topological surface roughness is described in⁵¹. Roughness profiles were generated using a jagged granular generator algorithm. Equally spaced coefficients at 50 nm spacing in the x-y plane are randomly generated. The remaining coefficients are obtained using bi-linear interpolation from the randomly generated points. The resulting array of coefficients in the x-y plane are used to locally multiply the base parameter values, M_S and K_u , or to obtain a topographical surface roughness profile – see Fig. 6. Further details are given in the user manual for Boris⁵³. Simulations with a thermal field at room temperature were done using the stochastic LLG equation, evaluated using Heun's method, with a thermal field obtained as:

$$|\mathbf{H}_{thermal}|_{max} = \sqrt{\frac{2k_B T}{\alpha \gamma \mu_0 M_S^0 V \Delta t}},$$

where V is the computational cell volume, Δt is the time step, and T is the temperature. The interfacial DMI effective field is introduced as shown below, where M_x, M_y, M_z are the components of magnetisation:

$$\mathbf{H} = -\frac{2D}{\mu_0 M_S^2} \left(\frac{\partial M_z}{\partial x}, \frac{\partial M_z}{\partial y}, -\frac{\partial M_x}{\partial x} - \frac{\partial M_y}{\partial y} \right)$$

Data Availability

The datasets generated during and/or analysed during the current study are available from the corresponding author on reasonable request.

References

- Nagaosa, N. & Tokura, Y. Topological properties and dynamics of magnetic skyrmions. *Nature Nanotechnology* **8**, 899–911 (2013).
- McVitie, S. *et al.* A transmission electron microscope study of Néel skyrmion magnetic textures in multilayer thin film systems with large interfacial chiral interaction. *Scientific Reports* **8**, 5703 (2018).
- Moreau-Luchaire, C. *et al.* Additive interfacial chiral interaction in multilayers for stabilization of small individual skyrmions at room temperature. *Nature Nanotechnology* **11**, 444–448 (2016).
- Boulle, O. *et al.* Room-temperature chiral magnetic skyrmions in ultra-thin magnetic nanostructures. *Nature Nanotechnology* **11**, 449–454 (2016).
- Zeissler, K. *et al.* Pinning and hysteresis in the field dependent diameter evolution of skyrmions in Pt/Co/Ir superlattice stacks. *Scientific Reports* **7**, 15125 (2017).
- Jiang, W. *et al.* Blowing magnetic skyrmion bubbles. *Science* **349**, 283–286 (2015).
- Woo, S. *et al.* Observation of room-temperature magnetic skyrmions and their current-driven dynamics in ultra-thin metallic ferromagnets. *Nature Materials* **15**, 501–506 (2016).
- Legrand, W. *et al.* Room-temperature current-induced generation and motion of sub-100 nm skyrmions. *Nano Letters* **17**, 2703–2712 (2017).
- Jiang, W. *et al.* Direct observation of the skyrmion Hall effect. *Nature Physics* **13**, 162–169 (2017).
- Litzius, K. *et al.* Skyrmion Hall effect revealed by direct time-resolved X-ray microscopy. *Nature Physics* **13**, 170–175 (2017).
- Woo, S. *et al.* Current-driven dynamics and inhibition of the skyrmion Hall effect of ferrimagnetic skyrmions in GdFeCo films. *Nature Communications* **9**, 959 (2018).
- Hrabec, A. *et al.* Current-induced skyrmion generation and dynamics in symmetric bilayers. *Nature Communications* **8**, 15765 (2017).
- Zeissler, K. *et al.* Discrete Hall resistivity contribution from Néel skyrmions in multilayer nanodiscs. *Nature Nanotechnology* **13**, 1161–1166 (2018).
- Emori, S. B., Ahn, U., Min, S.-, Martinez, E. & Beach, G. S. D. Current-driven dynamics of chiral ferromagnetic domain walls. *Nature Materials* **12**, 611–616 (2013).
- Zhang, X., Zhou, Y. & Ezawa, M. Magnetic bilayer-skyrmions without skyrmion Hall effect. *Nature Communications* **7**, 10293 (2016).
- Barker, J. & Tretiakov, O. A. Static and Dynamical Properties of Antiferromagnetic Skyrmions in the Presence of Applied Current and Temperature. *Phys. Rev. Lett.* **116**, 147203 (2016).
- Hirata, Y. *et al.* Vanishing skyrmion Hall effect at the angular momentum compensation temperature of a ferrimagnet. *Nature Nanotechnology* **14**, 232–236 (2019).
- Gobel, B., Schaffer, A. F., Berakdar, J., Mertig, I. & Parkin, S. S. P. Electrical writing, deleting, reading, and moving of magnetic skyrmioniums in a racetrack device. arXiv:1902.06295v1 (2019).
- Zhang, S. & Li, Z. Roles of Nonequilibrium Conduction Electrons on the Magnetization Dynamics of Ferromagnets. *Phys. Rev. Lett.* **93**, 127204 (2004).
- Zhang, S., Levy, P. M. & Fert, A. Mechanisms of spin-polarized current-driven magnetization switching. *Phys. Rev. Lett.* **88**, 236601 (2002).
- Eliás, R. G., Vidal-Silva, N. & Manchon, A. Steady motion of skyrmions and domains walls under diffusive spin torques. *Phys. Rev. B* **95**, 104406 (2017).
- Sampaio, J., Cros, V., Rohart, S., Thiaville, A. & Fert, A. Nucleation, stability and current-induced motion of isolated magnetic skyrmions in nanostructures. *Nature Nanotechnology* **8**, 839844 (2013).
- Amin, V. P., Zemen, J. & Stiles, M. D. Interface-Generated Spin Currents. *Phys. Rev. Lett.* **121**, 136805 (2018).
- Dyakonov, M. I. Magnetoresistance due to edge spin accumulation. *Phys. Rev. Lett.* **99**, 126601 (2007).
- Lepadatu, S. Unified treatment of spin torques using a coupled magnetisation dynamics and three-dimensional spin current solver. *Scientific Reports* **7**, 12937 (2017).
- Zhang, S. Spin Hall effect in the presence of spin diffusion. *Phys. Rev. Lett.* **85**, 393–396 (2000).
- Brataas, A., Nazarov, Y. V. & Bauer, G. E. W. Finite-element theory of transport in ferromagnet-normal metal systems. *Phys. Rev. Lett.* **84**, 2481–2484 (1999).
- Tserkovnyak, Y., Brataas, A. & Bauer, G. E. W. Spin pumping and magnetization dynamics in metallic multilayers. *Phys. Rev. B* **66**, 224403 (2002).
- Zhang, W., Han, W., Jiang, X., Yang, S.-H. & Parkin, S. S. P. Role of transparency of platinum–ferromagnet interfaces in determining the intrinsic magnitude of the spin Hall effect. *Nature Physics* **11**, 496–502 (2015).
- Mann, W. S., Tan, M., Caretta, A. J. L. & Beach, G. S. D. Enhanced spin-orbit torques in Pt/Co/Ta heterostructures. *Appl. Phys. Lett.* **105**, 212404 (2014).
- Zhang, S., Zhang, J., Wen, Y., Chudnovsky, E. M. & Zhang, X. Creation of a thermally assisted skyrmion lattice in Pt/Co/Ta multilayer films. *Appl. Phys. Lett.* **113**, 192403 (2018).
- Wang, L. *et al.* Construction of a Room-Temperature Pt/Co/Ta Multilayer Film with Ultrahigh-Density Skyrmions for Memory Application. *ACS Appl. Mater. Interfaces* **11**, 12098–12104 (2019).
- Qiu, X. *et al.* Spin-orbit-torque engineering via oxygen manipulation. *Nature Nanotechnology* **10**, 333–338 (2015).
- Torrejon, J. *et al.* Interface control of the magnetic chirality in CoFeB/MgO heterostructures with heavy-metal underlayers. *Nature Communications* **5**, 4655 (2014).
- Thiele, A. A. Steady-state motion of magnetic domains. *Phys. Rev. Lett.* **30**, 230–233 (1973).
- Beaujour, J.-M. L., Lee, J. H., Kent, A. D., Krycka, K. & Kao, C.-C. Magnetization damping in ultra-thin polycrystalline Co films: Evidence for nonlocal effects. *Phys. Rev. B* **74**, 214405 (2006).
- Metaxas, P. J. *et al.* Creep and flow regimes of magnetic domain-wall motion in ultra-thin Pt/Co/Pt films with perpendicular anisotropy. *Phys. Rev. Lett.* **99**, 217208 (2007).
- Tomasello, R. *et al.* A strategy for the design of skyrmion racetrack memories. *Scientific Reports* **4**, 6784 (2014).
- Legrand, W. *et al.* Hybrid chiral domain walls and skyrmions in magnetic multilayers. *Science Advances* **4**, eaat0415 (2018).
- Li, W. *et al.* Anatomy of Skyrmionic Textures in Magnetic Multilayers. *Advanced Materials* **31**, 1807683 (2019).
- Iwasaki, J. *et al.* Colossal spin transfer torque effect on skyrmion along the edge. *Nano Letters* **14**, 4432–4437 (2014).
- Reichhardt, C., Ray, D. & Reichhardt, C. J. O. Collective transport properties of driven skyrmions with random disorder. *Phys. Rev. Lett.* **114**, 217202 (2015).
- Reichhardt, C. & Reichhardt, C. J. O. Noise fluctuations and drive dependence of the skyrmion Hall effect in disordered systems. *New J. Phys.* **18**, 095005 (2016).
- Kim, J.-V. & Yoo, M.-W. Current-driven skyrmion dynamics in disordered films. *Appl. Phys. Lett.* **110**, 132404 (2017).
- Salimath, A., About, A., Brataas, A. & Manchon, A. Current-driven skyrmion depinning in magnetic granular films. *Phys. Rev. B* **99**, 104416 (2019).
- Raposo, V., Martinez, R. F. L. & Martinez, E. Current-driven skyrmion motion along disordered magnetic tracks. *AIP Advances* **7**, 056017 (2017).
- Wang, W., Beg, M., Zhang, B., Kuch, W. & Fangohr, H. Driving magnetic skyrmions with microwave fields. *Phys. Rev. B* **92**, 020403 (2015).

48. Tomasello, R. *et al.* Micromagnetic understanding of the skyrmion Hall angle current dependence in perpendicularly magnetized ferromagnets. *Phys. Rev. B* **98**, 224418 (2018).
49. Schütte, C., Iwasaki, J., Rosch, A. & Nagaosa, N. Inertia, diffusion, and dynamics of a driven skyrmion. *Phys. Rev. B* **90**, 174434 (2014).
50. Miltat, J., Rohart, S. & Thiaville, A. Brownian motion of magnetic domain walls and skyrmions, and their diffusion constants. *Phys. Rev. B* **97**, 214426 (2018).
51. Lepadatu, S. Effective field model of roughness in magnetic nano-structures. *Journal of Applied Physics* **118**, 243908 (2015).
52. Belusky, M., Lepadatu, S., Naylor, J. & Vopson, M. M. Evidence of substrate roughness surface induced magnetic anisotropy in Ni80Fe20 flexible thin films. *J. Magn. Magn. Mater.* **478**, 77–83 (2019).
53. Boris Computational Spintronics freely available, <https://boris-spintronics.uk/download> User Manual, <https://doi.org/10.13140/RG.2.2.31496.88322> (21st March 2019).
54. Ghosh, A., Auffret, S., Ebels, U. & Bailey, W. E. Penetration Depth of Transverse Spin Current in Ultrathin Ferromagnets. *Phys. Rev. Lett.* **109**, 127202 (2012).
55. Petitjean, C., Luc, D. & Waintal, X. Unified drift-diffusion theory for transverse spin currents in spin valves, domain walls, and other textured magnets. *Phys. Rev. Lett.* **109**, 117204 (2012).
56. Bass, J. & Pratt, W. P. Jr. Spin-diffusion lengths in metals and alloys, and spin-flipping at metal/metal interfaces: an experimentalist's critical review. *J. Phys. Cond. Mat.* **19**, 183201 (2007).
57. Montoya, E. *et al.* Spin transport in tantalum studied using magnetic single and double layers. *Phys. Rev. B* **94**, 054416 (2016).
58. Halbritter, A., Geresdi, A. & Mihalý, G. Spin polarized transport as measured by superconducting Andreev spectroscopy. *Frontiers in Nanoscience and Nanotechnology* **2**, 1–8 (2016).
59. Perez-Willard, F. *et al.* Determining the current polarization in Al/Co nanostructured point contacts. *Phys. Rev.* **69**, 140502 (2004).
60. Piraux, L., Dubois, S., Fert, A. & Belliard, L. The temperature dependence of the perpendicular giant magnetoresistance in Co/Cu multilayered nanowires. *Eur. Phys. J. B* **4**, 413–420 (1998).
61. Liu, L. *et al.* Spin-Torque Switching with the Giant Spin Hall Effect of Tantalum. *Science* **336**, 555–558 (2012).

Author Contributions

S.L. planned the work, implemented the model, performed the simulations, analysed the results and wrote the manuscript.

Additional Information

Supplementary information accompanies this paper at <https://doi.org/10.1038/s41598-019-46091-1>.

Competing Interests: The author declares no competing interests.

Publisher's note: Springer Nature remains neutral with regard to jurisdictional claims in published maps and institutional affiliations.



Open Access This article is licensed under a Creative Commons Attribution 4.0 International License, which permits use, sharing, adaptation, distribution and reproduction in any medium or format, as long as you give appropriate credit to the original author(s) and the source, provide a link to the Creative Commons license, and indicate if changes were made. The images or other third party material in this article are included in the article's Creative Commons license, unless indicated otherwise in a credit line to the material. If material is not included in the article's Creative Commons license and your intended use is not permitted by statutory regulation or exceeds the permitted use, you will need to obtain permission directly from the copyright holder. To view a copy of this license, visit <http://creativecommons.org/licenses/by/4.0/>.

© The Author(s) 2019